Chapter 12

Model Evaluation

12.1 Evaluation Criteria

Six basic requirements must be met before the credibility of simulations performed with that a mesoscale numerical model can be established by the scientific community. In reading papers in the published literature, one must consider the same criteria when evaluating the results and conclusions of those papers. These requirements are as follows.

1. The model must be compared with known analytic solutions. To perform these experiments, the mesoscale model is forced by very small perturbations, so that essentially linearized results are produced, or the initial and boundary conditions are idealized, so that exact solutions to the nonlinear equations are possible.

2. Nonlinear simulations with the model must be compared with the results from other models that have been developed independently.

3. The mass, moisture, and energy budgets of the model must be computed to determine the conservation of these important physical quantities.

4. The model predictions must be quantitatively compared with observations.

5. The computer logic of the model must be available on request, so that the flow structure of the code can be examined.

6. The published version of the model must have been subjected to peer review. For this reason, model results presented in recognized professional journals (e.g., *Monthly Weather Review, The Journal of Atmospheric Science, The Quarterly Journal of the Royal Meteorological Society, Tellus, The Journal of the Meteorological Society of Japan, The Chinese Journal of Atmospheric Sciences, Atmosfera, Atmosphere-Ocean, Boundary-Layer Meteorology, The Journal of Geophysical Research, Meteorology and Atmospheric Physics, Russian Meteorology and Hydrology*) should carry more weight than those distributed in report formats.

Hanna (1994) provides a similar list of evaluation criteria. In this chapter, several of these criteria are examined in more detail.

12.2   Comparison with Analytic Theory

To compare a numerical model with its analytic analog, the equations in the computational model must be used in the same form as used to develop the solution for the analytic version. Except for special cases, the development of an analogous system of equations in a numerical model usually requires that the equations be linearized. In addition, to minimize computational errors, the grid resolution of the model must be sufficiently small such that the spatial scale of the forcing (e.g., L_x and L_z) are adequately resolved, as summarized in Chapter 10, Section 10.6.

Figure 12-1, reproduced from Martin (1981), illustrates a numerical simulation performed to validate the model against Defant's (1950) exact linear
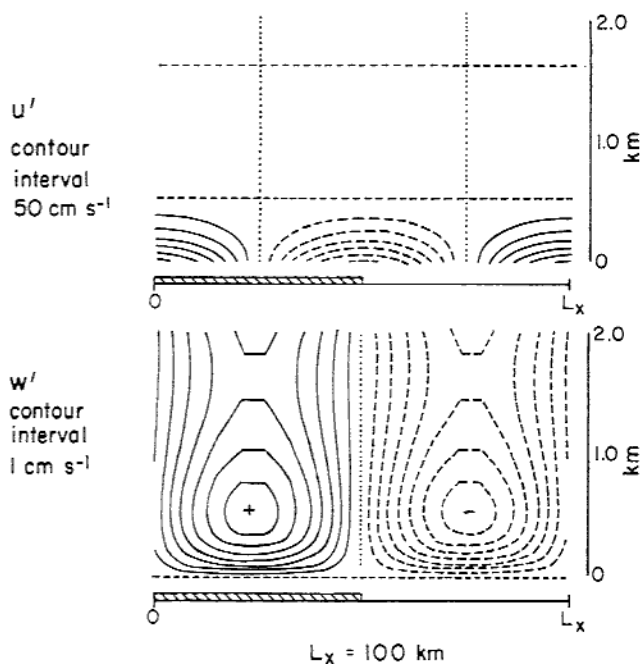

Fig. 12-1. The horizontal and vertical velocity fields 6 hours after sunrise predicted by a numerical model analog to Defant's (1950) analytic model. The input parameters are given by Eq. (5-99), the results correspond to the exact solution given in Figure 5-4. (From Martin 1981.)

solution. Defant's analytic model was derived in Chapter 5, Section 5.2.3.1. Although there are minor differences between the fields in Figure 12-1 and those evaluated from Defant's solution (e.g., Figure 5-4), the solutions are almost identical.

Klemp and Lilly (1978) have performed similar comparisons between analytic and numerical solutions for airflow over rough terrain. One example is reproduced in Figure 12-2. In addition to validations against linear theory, Klemp and Lilly (1978) and Lilly and Klemp (1979) also performed comparisons against analytic solutions of a subset set of the nonlinear conservation equations developed by Long (1953, 1955); see Section 5.3 for a derivation of the Long model. Although Long's solutions are valid only for the special case when the flow is steady state and the density multiplied by the domain-averaged horizontal velocity squared is independent of height, such comparisons offer some evidence of the accuracy of the numerical computations. The limitations of Long's solution to actual stratified flows over an obstacle are discussed by Baines (1977). Durran (1981) has referenced studies by other investigators who obtained exact solutions for specialized sets of the nonlinear conservation equations.
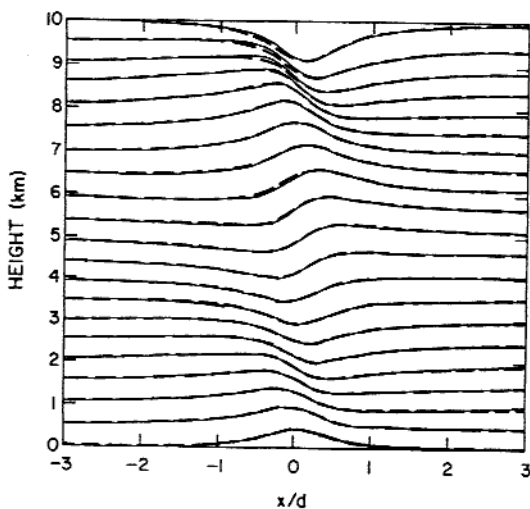

Fig. 12-2. Comparison of predicted contours of potential temperature $\bar{\theta}$ for an analytic solution (dashed line) and the equivalent numerical solution (solid line) for a bell-shaped mountain of 10 m. Results have been amplified by 50 for illustration purposes. The normalizing factor d is the characteristic half-width of the mountain. The atmosphere in this simulation was prescribed as isothermal initially with a large-scale wind flow of 20 m s^{-1}, constant with height. (From Klemp and Lilly 1978.)

12.3 Comparison with Other Numerical Models

In evaluating a numerical model, it is useful to compare its results for a particular simulation with those of a model from a different set of investigators, such as reported by Cox *et al.* (1998). Although all models start with the conservation equations discussed in Chapter 2, such model facets as the computational schemes, parameterizations, and particular simplified form of the conservation equations result in different model formulations. Although similar model results do not necessarily indicate a realistic reproduction of the actual atmospheric system, they are useful experiments to ascertain whether independent researchers using different model structures can replicate each others' results.

Mahrer and Pielke (1977b) performed a qualitative evaluation of their three-dimensional simulation of the airflow over the White Sands Missile Range in New Mexico against that of Anthes and Warner (1974), but used no quantitative measures of degree of agreement. Tapp and White (1976), Hsu (1979), and MacDonald *et al.* (2000) performed a similar qualitative comparison of their results against the sea-breeze simulation reported in Pielke (1974a). An example of an intercomparison between the results of Tapp and White (1976) and of Pielke (1974a) are illustrated in Figure 12-3. Carpenter and Lowther (1981) have shown that these Florida sea-breeze results are relatively insensitive to changes

HORIZONTAL VELOCITY
ANGLE = 135.   LEVEL = 0.05 km

WIND VECTORS
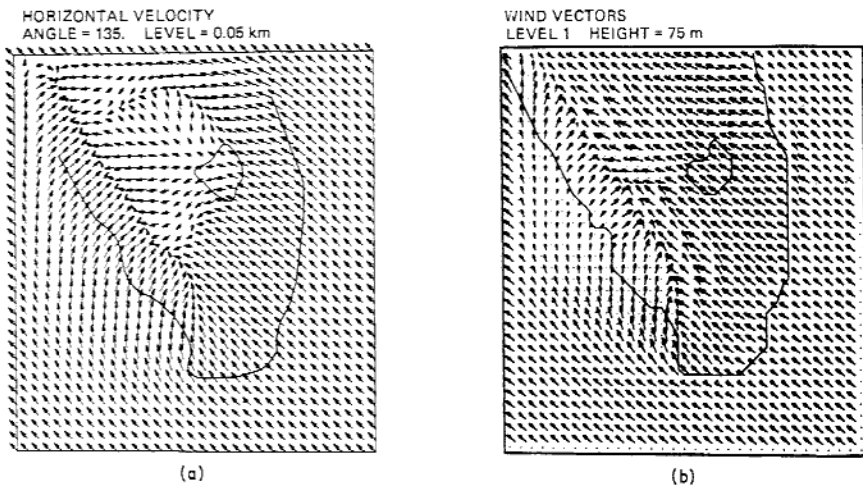LEVEL 1   HEIGHT = 75 m

(a)

(b)

Fig. 12-3. The predicted horizontal winds (a) at 50 m, 10 hours after sunrise (Pielke 1974a) and (b) at 75 m, 12 hours after sunrise (Tapp and White 1976). The synoptic geostrophic wind for both simulations was from the southeast to 6 m s^{-1}, and the maximum land-surface temperature during the day was 10°C warmer than the surrounding ocean temperature. The distance between one grid point (indicated by the origin of the arrows) corresponds to 6 m s^{-1}.

in the vertical grid mesh used. This result is consistent with the two-dimensional vertical grid resolution sensitivity test illustrated in Chapter 11, Figure 11-6.

Using two-dimensional models, Kessler and Pielke (1982), Mahrer and Pielke (1978b), and Peltier and Clark (1979) have simulated the airflow over rough terrain for the Colorado Front Range windstorm of January 11, 1972 (described by Lilly and Zipser 1972), and compared their results to those of Klemp and Lilly (1978). A more recent model intercomparison of the simulations of this wind storm, using 11 different models, is reported in Doyle et al. (2000).

12.4   Comparison Against Different Model Formulations

Rather than comparing results from models of different investigators, one can examine alternative forms of the same model. In one form of *sensitivity* study,[1] changes to the model can include different computational schemes, other approximations to the conservation equations, and so on. Tapp and White (1976), for example, contrasted the use of forward-in-time, upstream differencing (Scheme I in Table 10-1) of the advective terms in their sea-breeze model with the use of a second-order leapfrog representation (Scheme II in Table 10-1). Although the results were similar, the use of upstream differencing produced smoother vertical and horizontal velocity fields. The noisier fields resulting from the leapfrog representation may have occurred due to the poor handling of phase speed with that scheme. Mahrer and Pielke (1978b) performed a test of the upstream spline interpolation (Scheme III in Table 10-1) and the upstream differencing in a two-dimensional sea-breeze simulation and found no significant differences in the results. (In the same paper, however, Mahrer and Pielke found that the upstream differencing scheme produced mountain wave solutions with excessive damping, as contrasted with the more realistic appearing solutions obtained with the spline. Sea-breeze simulations can produce reasonable solutions with upstream differencing because such a mesoscale feature is strongly controlled by vertical subgrid-scale mixing, whereas simulations of forced airflow over rough terrain require a much more accurate representation of advection and gravity wave propagation.)

The evaluation of nonlinear model results with and without the hydrostatic assumption is of particular interest. For the sea-breeze circulation, Pielke (1972), Martin (1981), and Martin and Pielke (1983) examined the relative magnitude of the nonhydrostatic pressure in a nonlinear model in considerable depth. One procedure used to evaluate this pressure is to derive a Poisson equation for the hydrostatic component of the pressure, $\bar{p}_H = p'_H + p_0$, as was performed for the Defant sea-breeze model in Section 5.2.3.2. The difference between the total

and hydrostatic pressure, defined here as R', represents a grid-volume–averaged nonhydrostatic pressure residual. In an anelastic formulation, since $\partial p_0/\partial x_i$ is already required to be in hydrostatic balance, the ratio given by

$$\left.\left|\frac{\partial p'_H}{\partial x_i} + \frac{\partial R'}{\partial x_i}\right|\middle/\left|\frac{\partial p'_H}{\partial x_i}\right|\right., \qquad i = 1, 2, \tag{12-1}$$

indicates the significance of the nonhydrostatic effect.

To illustrate the derivation of R' for a nonlinear model, assume that the depth of the atmospheric circulation of interest is much smaller than the density scale depth of the atmosphere (i.e., $L_z \ll H_a$) so that the shallow continuity equation in (4-23) can be used, the second term on the left of Eq. (4-35) can be ignored, and α'/α_0 can be approximated by θ'/θ_0. In addition, to simplify the analysis (without losing the generality of the result since p_0 is assumed hydrostatically determined) assume $(\partial/\partial x_i)p_0 = 0 \,(i = 1, 2)$. For this situation, differentiating Eq. (4-34) with respect to z and Eq. (4-14) with respect to x and y (i.e., $\partial/\partial x_i$ with $i = 1, 2$), where $\bar{p}$ is replaced with $\bar{p}_H$, and adding the two equations yields

$$\left(\frac{\partial^2}{\partial x^2} + \frac{\partial^2}{\partial y^2} + \frac{\partial^2}{\partial z^2}\right)p'_H = \nabla^2 p'_H = \frac{\partial^2}{\partial x_i\partial x_j}\rho_0\bar{u}_i\bar{u}_j$$

$$- \frac{\partial^2}{\partial x_i\partial x_j}\rho_0\overline{u''_j u''_i} - 2\rho_0\epsilon_{ijk}\Omega_j\frac{\partial}{\partial x_i}\bar{u}_k$$

$$- \frac{\partial}{\partial x_i}\rho_0\frac{\partial \bar{u}_i^*}{\partial t} + g\frac{\partial}{\partial z}\rho_0\frac{\theta'}{\theta_0} \quad (i = 1, 2), \tag{12-2}$$

where $\partial \bar{u}_i^*/\partial t$ is evaluated from Eq. (4-14) using $\bar{p}_H$ in place of the total pressure $\bar{p}$. Subtracting Eq. (12-2) from the form of Eq. (4-35) for a shallow atmospheric system and with $\partial p_0/\partial x_i \,(i = 1, 2) = 0$, and assuming that the velocities occurring in Eq. (12-2) that do not involve a time tendency term are the same as the equivalent velocities in Eq. (4-35), results in the equation[2]

$$\frac{\partial^2 R'}{\partial x_i^2} = -\frac{\partial^2}{\partial z\partial x_j}\rho_0\bar{u}_j\bar{w} - \frac{\partial^2}{\partial z\partial x_j}\rho_0\overline{u''_j w''} + \frac{\partial}{\partial x}\rho_0\frac{\partial \bar{u}^*}{\partial t} + \frac{\partial}{\partial y}\rho_0\frac{\partial \bar{v}^*}{\partial t}, \tag{12-3}$$

where $R' = \bar{p} - \bar{p}_H = p' - p'_H$. Since the magnitude of $\partial/\partial x_i$ in Eq. (12-1) is over the same distance for each term, examination of

$$\epsilon = |R'/p'_H|$$

at each grid point over a model simulation is an adequate test of the adequacy of the hydrostatic assumption.

Pielke (1972) found for sea-breeze simulations that for the same scale of horizontal heating, ϵ became larger as the heating was increased and as the thermodynamic stratification was made less stable. This result agrees with that found by Martin for the linear model results discussed in Section 5.2.3 and

illustrated in Figures 5-5 and 5-6. The variation of the maximum nonhydrostatic pressure residual as a function of heat input and overlying stratification from Pielke's (1972) results are illustrated in Figure 12-4 as a function of the horizontal grid scale used. For each experiment, heat was input within the lowest 300 m over a horizontal distance of $9\Delta x$ and over a time scale such that the maximum heating was reached at the time indicated at the top of the figure. Even for relatively small scales of horizontal heating over short time periods (e.g., with $L_x = 9$ km, the time to maximum heating was 30 min), the hydrostatic relation appears to be a valid assumption for the pressure distribution.

Figures 12-5 and 12-6 illustrate results from Pielke (1972) for a hydrostatic model run, where p'_H is used to represent the horizontal pressure gradient, and for a nonhydrostatic simulation, where $p' = p'_H + R'$ is used for that horizontal gradient. The scales of horizontal heating in the calculation are 2.7 and 9 km, with a maximum temperature amplitude, $\Delta\bar\theta_{max}$, in Eq. (11-30) of $5°$, and a potential temperature gradient in the lowest 2.7 km of the model of $1°C/300$ m. In Figures 12-5 and 12-6, day in Eq. (11-30) was defined as 2160 s and
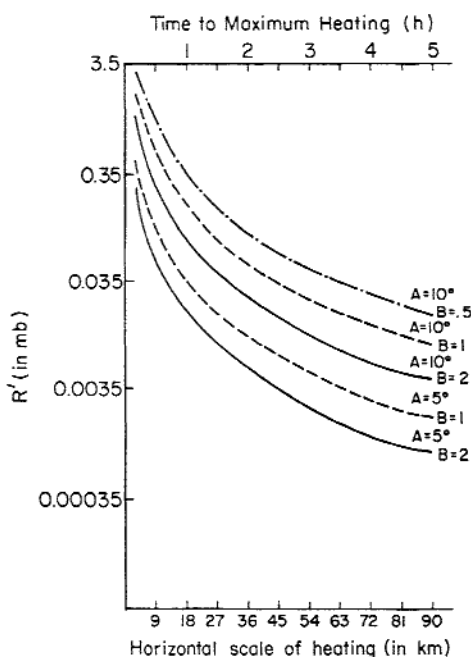

Fig. 12-4. The maximum absolute value of the nonhydrostatic pressure residual, R', as a function of horizontal scale of heating and time to maximum heating (Pielke 1972). To determine R' from Pielke (1972:26), a large-scale pressure of 1000 mb was used. The magnitude of maximum heating is A [i.e., using $A = \Delta\bar\theta_{max}$ in Eq. (11-30)] and B is the value of $\partial\theta_0/\partial z$ in the middle and lower levels of the model in terms of $B°C/300$ m.
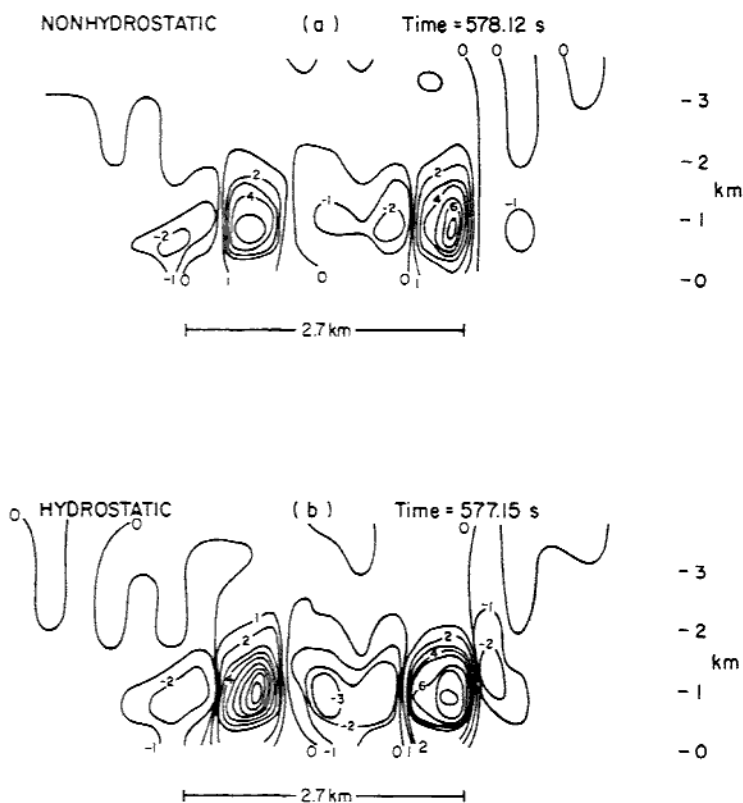
Fig. 12-5. The vertical velocity in centimeters per second in (a) an anelastic, nonhydrostatic model and (b) a hydrostatic model, where $L_x = 2.7$ km, $\Delta x = 0.3$ km, $\Delta \bar{\theta}_{max}$ and day in Eq. (11-30) of 5°C and 2160 s, and $\partial \theta_0 / \partial z = 1°C/300$ m in the lowest 2.7 km. The horizontal scale of heating is indicated at the bottom. (From Pielke 1972.)

7200 s, respectively. Despite the short time period of heat input, however, the differences between the hydrostatic and nonhydrostatic simulations for $L_x = 9$ km were small. With $L_x = 2.7$ km, the hydrostatic solution had substantially larger amplitude, although the locations of the convergence zones were similar. Figure 12-7 illustrates the contribution of the nonhydrostatic pressure residual, R', to the total pressure for Pielke's (1972) sea-breeze calculations. In a nonhydrostatic model, the vertical accelerations act to diminish the magnitude of the hydrostatic horizontal pressure gradients.

Martin's (1981) study substantiated Pielke's (1972) investigation of the relative influence of the nonhydrostatic pressure residual. In Martin's thesis, the nonlinear advection terms are added to Defant's (1950) analytic equations given
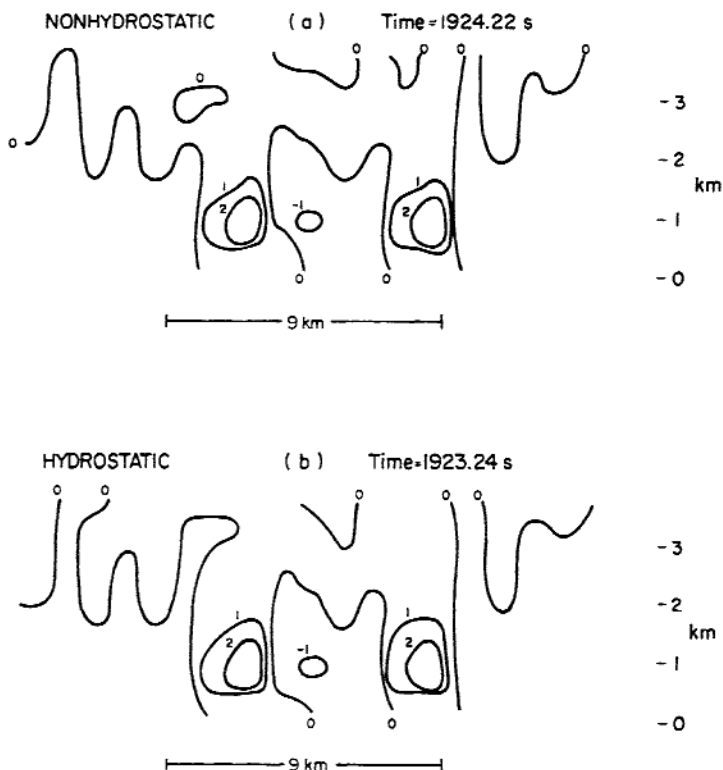
NONHYDROSTATIC   (a)   Time = 1924.22 s

HYDROSTATIC   (b)   Time = 1923.24 s

Fig. 12-6. Same as Figure 12-5 except $L_x = 9$ km and day = 7200 s. (From Pielke 1972.)

by Eqs. (5-66)–(5-70); that is, $u' \partial u'/\partial x$ and $w' \partial u'/\partial z$ to Eq. (5-66), $u' \partial v'/\partial x$ and $w' \partial v'/\partial z$ to Eq. (5-67), $u' \partial w'/\partial x$ and $w' \partial w'/\partial z$ to Eq. (5-68), and $u' \partial \theta'/\partial x$ and $w' \partial \theta'/\partial z$ to Eq. (5-70). A hydrostatic model is formed from these equations using $\partial p'_H/\partial z = \rho_0 \theta'/\theta_0$ in place of Eq. (5-68) (i.e., $\lambda_1 = 0$), and a nonhydrostatic version is derived of the form given by Eq. (12-3) where $p' = p'_H + R'$ is used in Eqs. (5-66) and (5-68) with $\lambda_1 = 1$. Figure 12-8 illustrates predicted results for horizontal velocity at the time of maximum heating, where $L_x = 6.25$ km and the largest temperature perturbation is 2.5°C. As in Pielke's (1972) earlier study, the nonhydrostatic and hydrostatic results are similar even for this relatively small spatial scale of heating.

Tag and Rosmond (1980) extended the hydrostatic–nonhydrostatic comparison to a three-dimensional cloud simulation. Among their findings was that moist processes magnified the nonhydrostatic effect, although increasing the stability from 1 to 2°C km^{-1} almost eliminated the differences caused by the nonhydrostatic effect.

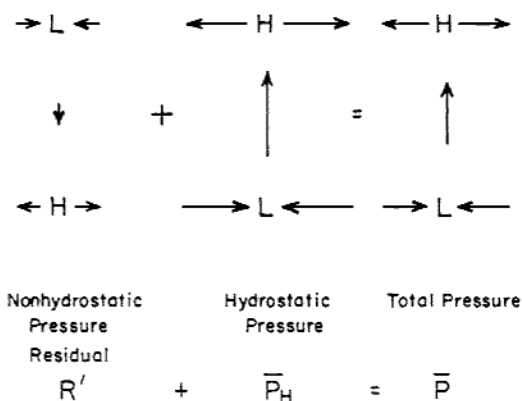$$R' \quad + \quad \overline{P}_H \quad = \quad \overline{P}$$

Fig. 12-7. A schematic of the relative contributions of the nonhydrostatic pressure residual and the hydrostatic pressure to the total pressure at a location over land in the center of the lowest pressure in the sea-breeze convergence zone. The arrows illustrate the instantaneous horizontal winds that would be expected from these pressure distributions. (Adapted from Pielke 1972.)

One of the advantages of using Eq. (12-3) to compute the nonhydrostatic pressure residual is that it must be computed only in a region where significant vertical accelerations exist. As illustrated in Figure 12-9, the boundary condition for R on the subdomain is straightforward to apply, since $R = 0$ where the motions are hydrostatic.

The importance of the nonhydrostatic residual has also been examined, to some extent, for forced air over rough terrain. Figure 12-10, reproduced from Durran (1981), shows potential temperature surfaces from one of Klemp and
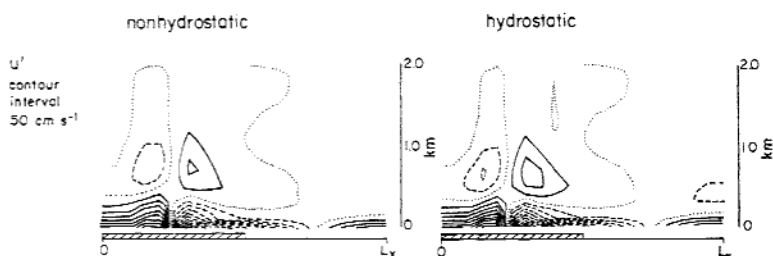

Fig. 12-8. Nonhydrostatic and hydrostatic simulations for $L_x = 6.25$ km after 2700 s with a surface heating function of $\hat{\theta} = \theta_0(t = 0) + |\Delta\theta|_{max} \sin(2\pi x/L_x) \sin(\pi t/T)$, where $|\Delta\theta|_{max} = 2.5°C$ and $T = 3$ h. The horizontal and vertical grid spacings were $\Delta x = 0.306$ km and $\Delta z = 100$ m. Periodic lateral boundary conditions were used. Other prescribed values include $\partial\theta_0/\partial x = 10°C$ km^{-1}, $K_\theta = 10$ m^2 s^{-1}, $f = 1.301 \times 10^{-4}$ s^{-1}, and σ_H and $\sigma_v = 10^{-3}$ s^{-1}. (These symbols are explained in Section 5.2.3.1.) Positive values are given by the solid line and negative values are represented by dashed lines, with 0 indicated by the dotted line. (From Martin 1981.)
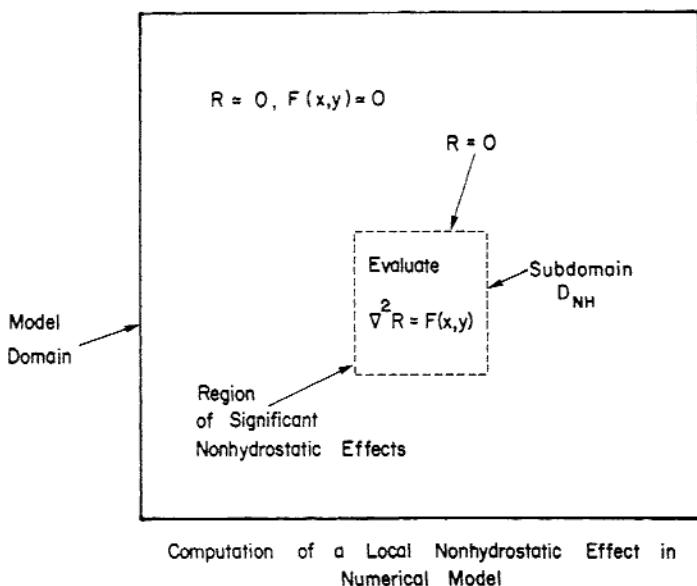
Computation   of   a   Local   Nonhydrostatic   Effect   in
Numerical   Model

Fig. 12-9. The definition of a subdomain, D_{NH}, in a model where nonhydrostatic effects are significant. Such a domain is defined to enclose those regions where $F(x, y)$ is significantly different from 0.

Lilly's (1978, Figure 10) hydrostatic simulations and an equivalent result performed by Durran for a nonhydrostatic simulation. In both model runs the upstream wind was 20 m s^{-1}, constant with height, the mountain height reached 1 km, $\partial\theta_0/\partial z = 4°$C km^{-1} within the lowest 10 km, and an isothermal absorbing layer (see Section 11.3.2 and Figure 11-18) was prescribed between 10 and 20 km in height. The half-width of the mountain was 20 km, where the terrain was defined as

$$z_G = b^2 z_{G_{\max}}/(x^2 + b^2), \qquad (12\text{-}4)$$

where b is the half-width and $z_{G_{\max}}$ is the maximum height of the terrain. Although the nonhydrostatic simulation produced a slightly steeper wave in the upper stratosphere, the hydrostatic and nonhydrostatic results are almost identical. Klemp and Lilly (1980) concluded that for realistic atmospheres with simple, uniform structure (i.e., constant large-scale velocity and static stability with height), ratios of $(b/|u_0|)[(g/\theta_0)(\partial\theta_0/\partial z)]^{1/2} \geq 10$ or so yield nearly identical hydrostatic and nonhydrostatic results. For example, with $\partial\theta_0/\partial z = 1$ K 100 m^{-1}, $\theta_0 = 300$ K, and $u_0 = 20$ m s^{-1}, $b \geq 10$ km or so satisfies this requirement. For a more general atmospheric structure, however, it is desirable to check the hydrostatic assumption for each situation.
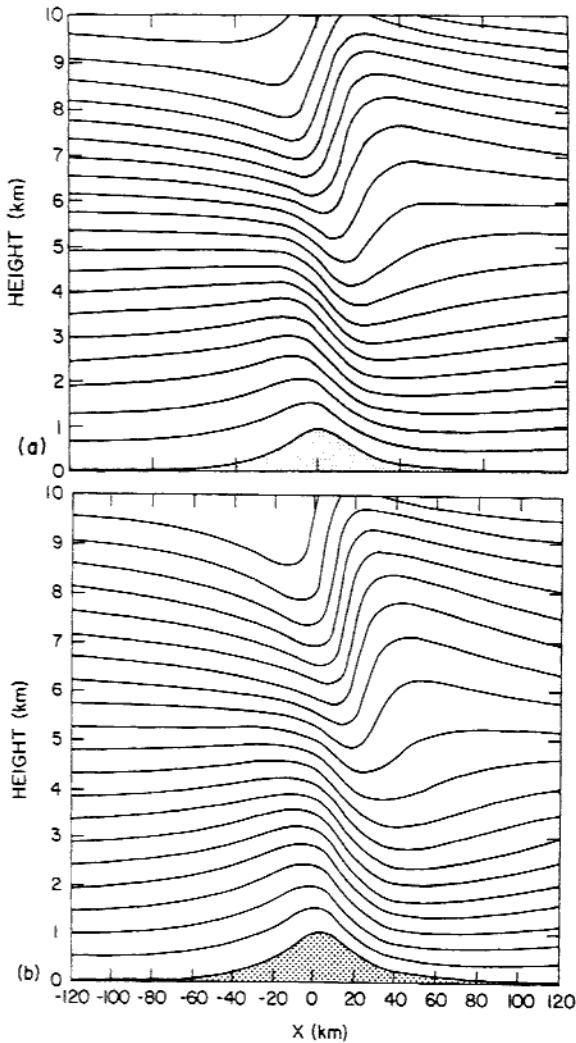
Fig. 12-10. Contours of potential temperature from (a) a nonlinear hydrostatic sim-
ulation by Klemp and Lilly (1978), and (b) a nonlinear nonhydrostatic simulation by
Durran (1981). The upstream winds were 20 m s^{-1}, and the upstream stratification within
the lowest 10 km was 4°C km^{-1}. Note that because of scale differences the height scale
in (b) is about 8% larger than that in (a). To more quantitatively compare the two results,
measure the trough-to-crest difference for equivalent initial inflow potential tempera-
ture heights.

12.5   Calculation of Model Budgets

Evaluation of the budgets of such physical quantities as kinetic energy and mass is useful not only to improve our understanding of mesoscale physical processes, but also, as a diagnostic tool to examine the fidelity of the computer program logic. Before discussing such budgets of mesoscale models, it is useful to examine this approach with the single fluid tank model introduced in Section 5.2.1.1.

12.5.1   Mass and Energy Equations for the Homogeneous Tank Model

The mass budget for this simplified model given by Eqs. (5-17) and (5-20) is particularly easy to compute, since the fluid is assumed to be homogeneous. Using the product rule of differentiation and integrating Eq. (5-20) over the tank model domain, D_x, yields

$$\int_0^{D_x} \frac{\partial h}{\partial t}\, dx + \int_0^{D_x} \frac{\partial}{\partial x} u' h\, dx = \int_0^{D_x} \frac{\partial h}{\partial t}\, dx + u' h \Big|_0^{D_x} = 0.$$

If the sides of the tank $(x = 0, D_x)$ are rigid (i.e., $u'_0 = u'_{D_x} = 0$),[3] or if periodic boundary conditions for h and u' are used (i.e., $u'h$ at $x = 0$ is equal to $u'h$ at $x = D_x$), then

$$\int_0^{D_x} \frac{\partial h}{\partial t}\, dx = \frac{\partial}{\partial t} \int_0^{D_x} h\, dx = \frac{\partial \bar{h}}{\partial t} = 0,$$

so that the average height of the fluid must be constant in time. In a numerical model, the conservation of mass, as represented by the depth of the fluid, can be checked at each time step by

$$\bar{h} = \frac{1}{I_D} \sum_{i=1}^{I_D} h_i,$$

where I_D is the number of grid points. If $\Delta \bar{h}/\Delta t \neq 0$, then mass is not conserved.

The kinetic energy of the tank model can be computed by multiplying Eq. (5-17) by hu' and Eq. (5-20) by $u'^2/2$, yielding the two simultaneous partial differential equations

$$hu' \frac{\partial u'}{\partial t} + hu'^2 \frac{\partial u'}{\partial x} + ghu' \frac{\partial h'}{\partial x} = h \frac{\partial u'^2/2}{\partial t} + hu' \frac{\partial}{\partial x}\left(\frac{u'^2}{2}\right) + ghu' \frac{\partial h}{\partial x} = 0$$

$$\frac{u'^2}{2} \frac{\partial h}{\partial t} + \frac{u'^2}{2} u' \frac{\partial h}{\partial x} + \frac{u'^2}{2} h \frac{\partial u'}{\partial x} = \frac{u'^2}{2} \frac{\partial h}{\partial t} + \frac{u'^2}{2} \frac{\partial}{\partial x}(hu') = 0.$$

Adding these two equations using the product rule of differentiation and multiplying through by the constant density ρ_0 yields

$$\frac{\partial}{\partial t}\left(\rho_0 \frac{u'^2}{2}h\right) + \frac{\partial}{\partial x}\left(\rho_0 \frac{u'^2}{2}hu'\right) + \rho_0 g hu'\frac{\partial h}{\partial x} = 0, \qquad (12\text{-}5)$$

where $\rho_0(u'^2/2h)$ as units of kinetic energy per unit area.

The potential energy equation is obtained by multiplying Eq. (5-20) by $\rho_0 g h$, resulting in

$$\rho_0 g h\frac{\partial h}{\partial t} + \rho_0 g h\frac{\partial}{\partial x}hu' = \rho_0 g\frac{\partial h^2/2}{\partial t} + \rho_0 g h\frac{\partial u'h}{\partial x} = 0, \qquad (12\text{-}6)$$

where $\rho_0 g h^2/2$ has units of potential energy per unit area.

To obtain the total energy, add Eqs. (12-5) and (12-6) and rearrange, giving

$$\frac{\partial}{\partial t}\left[\rho_0 \frac{u'^2}{2}h + \rho_0 g\frac{h^2}{2}\right] + \frac{\partial}{\partial x}\left[hu'\left(\rho_0 \frac{u'^2}{2} + \rho_0 g h\right)\right] = 0. \qquad (12\text{-}7)$$

The first term on the left is the local change of total energy per unit area E, and the second term is proportional to the horizontal flux divergence of this energy per unit area.

Integrating this expression over the model domain (i.e., the size of the tank) gives

$$\int_0^{D_x} \frac{\partial E}{\partial t}\,dx = -hu'\left(\rho_0 \frac{u'^2}{2} + \rho_0 g h\right)\Bigg|_0^{D_x} = \frac{\partial}{\partial t}\int_0^{D_x} E\,dx = \frac{\partial E_0}{\partial t},$$

which is equal to 0 if the walls are rigid or if cyclic boundary conditions are applied. If $\partial E_0/\partial t = 0$, then total energy is conserved in the tank model. Thus numerical approximations of the tank model equations should also conserve total energy; that is, evaluating the approximate form for the first bracketed term on the left of Eq. (12-7) at each grid point and summing across the domain should yield a number that is identical at each time step. Thus simulations that differ significantly from such mass- and energy-conservation criteria are suspect, and results from them should be used cautiously, if at all.

12.5.2 Mass and Energy Equations for a Mesoscale Model

In mesoscale models, much more involved conservation relations are used; however, it is similarly desirable to conserve mass and energy. To illustrate the procedure, the hydrostatic, anelastic form of the equations given by Eqs. (6-87)–(6-90) and (6.93) with σ defined by Eq. (6-48) are used to derive the kinetic energy and mass-conservation relations.

The shallow-slope, hydrostatic form of Eq. (6-90) [Eq. (6-62)] can be differentiated with time and the order of operation reversed to yield

$$\frac{\partial}{\partial \tilde{x}^3} \frac{\partial \bar{\pi}}{\partial t} = \frac{g}{\bar{\theta}^2} \frac{s - z_G}{s} \frac{\partial \bar{\theta}}{\partial t}.$$

Integrating between $\tilde{x}^3 = 0$ and s_θ and rearranging yields[4]

$$\left.\frac{\partial \bar{\pi}}{\partial t}\right|_{z_G} = \left.\frac{\partial \bar{\pi}}{\partial t}\right|_{s_\theta} - g\frac{s - z_G}{s} \int_0^{s_\theta} \frac{1}{\bar{\theta}^2} \frac{\partial \bar{\theta}}{\partial t} d\tilde{x}^3, \qquad (12\text{-}8)$$

which is the same form as Eq. (11-25) except $z_G \neq 0$ in Eq. (12-8). The pressure tendency $\partial \bar{\pi}/\partial t|_{s_\theta}$ must be specified as a boundary condition [i.e., see after Eq. (11-22)], and the integrated term in Eq. (12-8) is evaluated using Eq. (6-90). Integrating the right side of Eq. (12-8) over the model domain gives[5]

$$\frac{1}{D_{\tilde{x}^1} D_{\tilde{x}^2}} \int_0^{D_{\tilde{x}^1}} \int_0^{D_{\tilde{x}^2}} \left.\frac{\partial \bar{\pi}}{\partial t}\right|_{z_G} \left(\frac{s - z_G}{s}\right)\left(\frac{s}{s - z_G}\right) d\tilde{x}^2 d\tilde{x}^1$$

$$= \frac{1}{D_{\tilde{x}^1} D_{\tilde{x}^2}} \frac{\partial}{\partial t} \int_0^{D_{\tilde{x}^1}} \int_0^{D_{\tilde{x}^2}} \bar{\pi}_* d\tilde{x}^2 d\tilde{x}^1 = \frac{\partial \Pi_*}{\partial t}. \qquad (12\text{-}9)$$

Values of $\partial \bar{\theta}/\partial t$ needed at $\tilde{x}^1 = 0$, $D_{\tilde{x}^1}$ and at $\tilde{x}^2 = 0$, $D_{\tilde{x}^2}$ are obtained from the assumed lateral boundary condition on $\bar{\theta}$ (see Section 11.3.1).

Since from Eq. (11-27) a change of π at the surface is equivalent to a change of mass above that level, Π_* in Eq. (12-9) provides the value of the average mass change per unit area over the model domain. This value of Π_* can be compared against the integrated value of $\overline{\Pi}_{z_G}$ computed directly from Eq. (6-62); that is,

$$\frac{\overline{\Pi}_{z_G}}{\partial t} = \frac{1}{D_{\tilde{x}^1} D_{\tilde{x}^2}} \frac{\partial}{\partial t} \int_0^{D_{\tilde{x}^1}} \int_0^{D_{\tilde{x}^2}} \bar{\pi}_{z_G} d\tilde{x}^2 d\tilde{x}^1,$$

where

$$\bar{\pi}_{z_G} = +g\frac{s - z_G}{s} \int_0^{s_\theta} \frac{d\tilde{x}^3}{\bar{\theta}} + \left.\overline{\Pi}\right|_{s_\theta}.$$

The difference $(\partial/\partial t)(\Pi_{z_G} - \Pi_*)$ is proportional to the mass loss.

A kinetic energy equation for the flow parallel to the terrain can also be derived from the set of equations. Since $\tilde{u}^1 = u$ and $\tilde{u}^2 = v$ from Eq. (6-34), multiplying Eq. (6-57) by $\rho_0\bar{\tilde{u}}^1(s - z_G)/s$ and Eq. (6-58) by $\rho_0\bar{\tilde{u}}^2(s - z_G)/s$, adding the two equations, and using the anelastic conservation-of-mass equation,

after multiplying by $\bar{k} = \frac{1}{2}(\bar{\tilde{u}}^1 \bar{\tilde{u}}^1 + \bar{\tilde{u}}^2 \bar{\tilde{u}}^2)$, results in the terrain-following kinetic energy equation

$$
\rho_0 \frac{s - z_G}{s} \frac{\partial \bar{k}}{\partial t} = -\frac{\partial}{\partial \tilde{x}^j} \rho_0 \frac{s - z_G}{s} \bar{\tilde{u}}^j \bar{k} - \bar{\tilde{u}}^1 \rho_0 \frac{s - z_G}{s} \overline{\tilde{u}^{j''} \frac{\partial \tilde{u}^{1''}}{\partial \tilde{x}^j}}
$$

$$
- \bar{\tilde{u}}^2 \rho_0 \frac{s - z_G}{s} \overline{\tilde{u}^{j''} \frac{\partial \tilde{u}^{2''}}{\partial \tilde{x}^j}} - \bar{\tilde{u}}^1 \rho_0 \frac{s - z_G}{s}
$$

$$
\times \left\{ \theta \frac{\partial \bar{\pi}}{\partial \tilde{x}^1} - g \frac{\sigma - s}{s} \frac{\partial z_G}{\partial x} \right\} - \bar{\tilde{u}}^2 \rho_0 \frac{s - z_G}{s}
$$

$$
\times \left\{ \theta \frac{\partial \bar{\pi}}{\partial \tilde{x}^2} - g \frac{\sigma - s}{s} \frac{\partial z_G}{\partial y} \right\} - \bar{\tilde{u}}^1 \rho_0 \frac{s - z_G}{s} \hat{f} \bar{\tilde{u}}^3. \quad (12\text{-}10)
$$

Equation (12.10) can be integrated over the model domain, yielding

$$
\frac{\partial K_*}{\partial t} = -\int_0^{s_\theta} \left\{ \int_0^{D_{\tilde{x}^2}} \rho_0 \frac{s - z_G}{s} \bar{\tilde{u}}^1 \bar{k} \Big|_0^{D_{\tilde{x}^1}} d\tilde{x}^2 + \int_0^{D_{\tilde{x}^1}} \rho_0 \frac{s - z_G}{s} \bar{\tilde{u}}^2 \bar{k} \Big|_0^{D_{\tilde{x}^2}} d\tilde{x}^1 \right.
$$

$$
+ \int_0^{D_{\tilde{x}^2}} \int_0^{D_{\tilde{x}^1}} \rho_0 \frac{s - z_G}{s} \left[\bar{\tilde{u}}^1 \overline{\tilde{u}^{j''} \frac{\partial \tilde{u}^{1''}}{\partial \tilde{x}^j}} + \bar{\tilde{u}}^2 \overline{\tilde{u}^{j''} \frac{\partial \tilde{u}^{2''}}{\partial \tilde{x}^j}} \right] d\tilde{x}^1 d\tilde{x}^2
$$

$$
+ \int_0^{D_{\tilde{x}^2}} \int_0^{D_{\tilde{x}^1}} \rho_0 \frac{s - z_G}{s} \left[\bar{\tilde{u}}^1 \bar{\theta} \frac{\partial \bar{\pi}}{\partial \tilde{x}^1} + \bar{\tilde{u}}^2 \bar{\theta} \frac{\partial \bar{\pi}}{\partial \tilde{x}^2} \right] d\tilde{x}^1 d\tilde{x}^2
$$

$$
- \int_0^{D_{\tilde{x}^2}} \int_0^{D_{\tilde{x}^1}} \rho_0 \frac{s - z_G}{s} \left[\bar{\tilde{u}}^1 g \frac{\sigma - s}{s} \frac{\partial z_G}{\partial x} + \bar{\tilde{u}}^2 g \frac{\sigma - s}{s} \frac{\partial z_G}{\partial y} \right] d\tilde{x}^1 d\tilde{x}^2
$$

$$
- \int_0^{D_{\tilde{x}^2}} \int_0^{D_{\tilde{x}^1}} \rho_0 \frac{s - z_G}{s} \bar{\tilde{u}}^1 \hat{f} \bar{\tilde{u}}^3 d\tilde{x}^1 d\tilde{x}^2 \right\} d\tilde{x}^3
$$

$$
+ \int_0^{D_{\tilde{x}^2}} \int_0^{D_{\tilde{x}^1}} \rho_0 \frac{s - z_G}{s} \bar{k}_{s_\theta} \frac{\partial s_\theta}{\partial t} d\tilde{x}^1 d\tilde{x}^2, \quad (12\text{-}11)
$$

where

$$
K_* = \int_0^{s_\theta} \int_0^{D_{\tilde{x}^1}} \int_0^{D_{\tilde{x}^2}} \left(\rho_0 \frac{s - z_G}{s} \bar{k} \right) d\tilde{x}^2 d\tilde{x}^1 d\tilde{x}^3.
$$

In deriving Eq. (12-11), the condition that $\bar{\tilde{u}}^3 = 0$ at z_G and s_θ has been used. The last term in Eq. (12-11) arises from Leibnitz's rule,[6] since s_θ is a function of time. Each of the variables in the last term is evaluated at s_θ.

The first two terms on the right side of Eq. (12-11) are proportional to the net flow of terrain-following kinetic energy through the sides of the model domain, and the next term represents the change in kinetic energy from subgrid-scale effects. The terms involving $\partial \bar{\pi}/\partial \tilde{x}^1$ and $\partial \bar{\pi}/\partial \tilde{x}^2$ are proportional to the conversion of potential to kinetic energy by cross-isobaric flow, and the expressions containing the gradients of terrain represent the conversion of potential

to kinetic energy through upslope and downslope flow. The next to last term in Eq. (12-11) (with $\hat{f}$) would not appear in a three-dimensional kinetic energy equation using the complete conservation-of-motion equation (i.e., without the hydrostatic assumption), since the Coriolis force arises solely because of a coordinate transformation (see Section 2.3) and thus cannot do work. Therefore, to have a physically consistent terrain-following energy equation, it is necessary to remove this term in Eq. (12-11) and in Eq. (6-87).

In using Eq. (12-11) to determine the total terrain-following kinetic energy changes, it is imperative that the approximation technique used to evaluate the individual terms in that expression be the same as that used in the original approximate form of the conservation relation [i.e., the approximated forms of Eqs. (6-60) and (6-61)] from which Eq. (12-11) was derived.

The time rate of change of terrain-following kinetic energy can also be evaluated directly at each individual grid point and then summed; that is,

$$
\frac{\partial K}{\partial t} = \int_0^{s_\theta} \int_0^{D_{\tilde{x}^2}} \int_0^{D_{\tilde{x}^2}} \rho_0 \frac{s - z_G}{s} \frac{\partial \bar{k}}{\partial t} \, d\tilde{x}^2 d\tilde{x}^1 d\tilde{x}^3
$$
$$
+ \int_0^{D_{\tilde{x}^2}} \int_0^{D_{\tilde{x}^1}} \rho_0 \frac{s - z_G}{s} \bar{k}_{s_\theta} \frac{\partial s_\theta}{\partial t} \, d\tilde{x}^1 d\tilde{x}^2 \tag{12-12}
$$

is used instead of Eq. (12-11) to obtain an estimate of the total terrain-following kinetic energy change. If the kinetic energy changes computed by the numerical approximation to this expression and the approximated form of Eq. (12-11) closely agree, then the modeler can be certain that mistakes, such as coding errors, are not causing significant sources of unexplained changes of kinetic energy. Note that since the last term is the same in Eqs. (12-11) and (12-12), there is no need to compute it for a comparison of K and K_*.

Anthes and Warner (1978) discuss the use of kinetic energy budgets in mesoscale models as a tool to check the model code, as well as to seek additional insight into the energetics of mesoscale systems. Among their results, they showed that the flux of kinetic energy through the side walls of a mesoscale model crucially affects the solutions in the interior. They conclude that because of the extreme sensitivity of mesoscale model results to domain size and the form of lateral boundary conditions, studies of the energetics of real-world mesoscale systems will be very difficult to perform and very sensitive to errors and small-scale variations of wind, potential temperature, and pressure at the model boundaries. Figure 12-11 illustrates the magnitude of individual terms as a function of time in a two-dimensional analog of Eq. (12-11), computed by Anthes and Warner for strong airflow over rough terrain. Of particular importance is the large magnitude of the boundary fluxes of kinetic energy through the west and east boundaries. Even small percentage errors in these terms can cause serious errors in the results, a conclusion illustrated in Table 11-1. In a
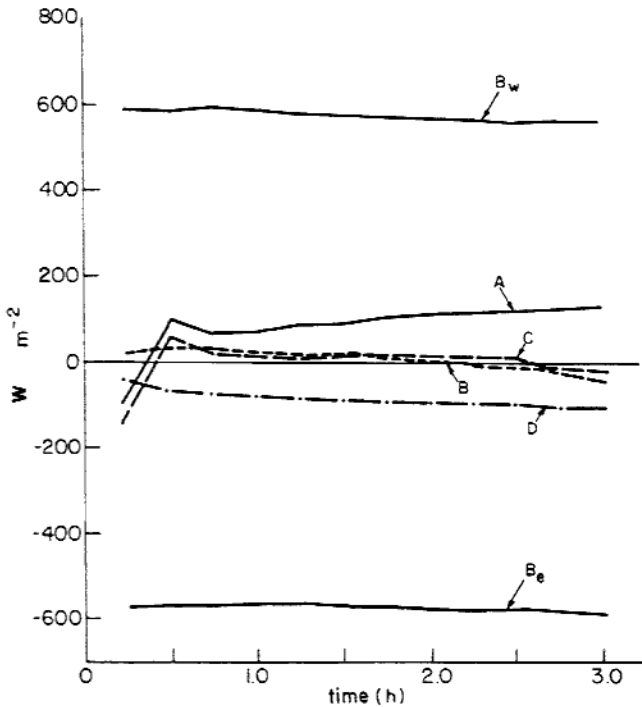
Fig. 12-11. ▪Individual components of a two-dimensional form of the domain-averaged kinetic energy equation, which is equivalent to Eq. (12-11). (A) Generation of kinetic energy by cross-isobaric flow, from the terms with $\bar{\tilde{u}}^1[\bar{\theta}(\partial\bar{\pi}/\partial\bar{x}^1) - g\{(\sigma - s)/s\}(\partial z_G/\partial x)]$; B_w and B_e are the flux of kinetic energy across the west and east boundaries from the two terms evaluated from $\bar{\tilde{u}}^1\bar{k}|_0^{D^i})$. (B) Net flux across the west and east boundaries (from $B_e - B_w$). (C) The domain-averaged change of kinetic energy. (D) The dissipation of kinetic energy by horizontal diffusion (from the term with $\bar{\tilde{u}}^1\overline{\tilde{u}^{1''}\partial\tilde{u}^{1''}/\partial\tilde{x}^1}$.). Analogs to the last two terms in Eq. (12-11) were not evaluated. (Reproduced from Anthes and Warner 1978.)

different study, Tag and Rosmond (1980) discuss energy conservation in a three-dimensional small-scale (nonhydrostatic) model in considerable detail. Pearson (1975), Dalu and Green (1980), and Green and Dalu (1980), provide additional studies of the energetics of mesoscale systems. Avissar and Chen (1993) use a mesoscale kinetic energy equation similar to Eq. (12-11) to develop a parameterization of mesoscale fluxes for use in larger-scale models.

12.5.3 Momentum Flux

Another useful diagnostic tool for model evaluation involves calculation of the momentum flux. Used most often in the study of the dynamics of forced air over rough terrain (e.g., Klemp and Lilly 1978), this is straightforward to calculate.

To illustrate its evaluation, in the absence of the Coriolis term for two-dimensional flow, Eq. (4-14) for $i = 1$ can be written as

$$\frac{\partial \rho_0 \bar{u}}{\partial t} = -\frac{\partial}{\partial x}\rho_0 \bar{u}^2 - \frac{\partial}{\partial z}\rho_0 \bar{w}\bar{u} - \frac{\partial}{\partial x}\rho_0 \overline{u''^2} - \frac{\partial}{\partial z}\rho_0 \overline{u''w''} - \frac{\partial \bar{p}}{\partial x}, \quad (12\text{-}13)$$

where the conservation-of-mass equation (4.23) has been used. Assuming a steady state and that $\bar{u}$, $\bar{p}$, and $\overline{u''^2}$, far enough upstream and downstream of a two-dimensional barrier to the flow, are constant, Eq. (12-13) can be integrated to yield

$$-\frac{\partial}{\partial z}\int_{-\infty}^{\infty}\left(\rho_0 \bar{w}\bar{u} + \rho_0 \overline{u''u''}\right) dx = 0$$

or

$$\int_{-\infty}^{\infty}\rho_0\left(\bar{w}\bar{u} + \overline{u''u''}\right) dx = m_1, \quad (12\text{-}14)$$

where m_1 is a constant with dimensions of kilogram per seconds squared. Equation (12.14) can be written as

$$\int_{-\infty}^{\infty}\rho_0\left[w_0 u_0 + w' u_0 + w_0 u' + w' u' + \overline{w''u''}\right] dx = m_1 \quad (12\text{-}15)$$

using the definition of a mesoscale perturbation from the domain-averaged (i.e., synoptic) value given by Eq. (4-11). For the case where $w_0 = 0$ and u_0 is equal to a positive constant, Eq. (12-15) reduces to

$$\int_{-\infty}^{\infty}\rho_0\left[w' u' + \overline{w''u''}\right] dx = m_2,$$

since $(\partial/\partial z)\rho_0 \bar{w}\bar{u}$ can be written as $(\partial/\partial z)\rho_0 w' u'$ in Eq. (12-13). Assuming nonturbulent flow, the equation can be further reduced to

$$\int_{-\infty}^{\infty}\rho_0 w' u' \, dx = m_3. \quad (12\text{-}16)$$

The constant m_3 is less than 0 if the source of the mesoscale motion is the ground surface and there is no downward reflection or generation of perturbed flow above the ground. In this situation, the movement of a parcel upward (i.e., $w' > 0$) toward a level of higher potential energy results in a reduction of kinetic energy (i.e., $u' < 0$). The converse is true for the downward movement of a parcel. Hence $w' u' < 0$ is required to satisfy the conservation of total energy.

Equation (12.16) is of the form most commonly applied in the diagnosis of a mesoscale simulation of airflow over rough terrain. In a numerical model, u_0 is equal to a constant, $w_0 = 0$, nonturbulent flow can be assumed for an atmosphere of constant large-scale velocity and static stability, and $w' u'$ can be calculated to ascertain whether it satisfies Eq. (12-16). To prevent aliasing problems (described in Section 10.5.1), however, long-term inviscid calculations (i.e., with no explicit or computational smoothing) can be performed only for

small mountain perturbations where the nonlinear effects are minimal. Klemp and Lilly (1978) show that for inviscid, isothermal analytic solutions over a bell-shaped mountain given by Eq. (12-4) with u_0 equal to a constant and $w_0 = 0$, the momentum flux is of the form

$$m_{3a} \simeq \frac{-\pi}{4} \rho_0 u_0 z_{G_{max}}^2 \left(\frac{g}{\theta_0} \frac{\partial \theta_0}{\partial z} \right)^{1/2} \simeq -\frac{\pi}{4} \rho_0 z_{G_{max}}^2 \sigma u_0^2. \qquad (12\text{-}17)$$

Here the definition of σ is from Eq. (5-129) and the relation between density and potential temperature vertical gradients is given by Eqs. (5-135) and (5-136). Figure 12-12, reproduced from Klemp and Lilly, illustrates a comparison of a numerically computed, horizontally integrated momentum flux [from Eq. (12-16)] for a simulation of airflow with $u_0 = 20$ m s^{-1} over a mountain of the form given by Eq. (12-4), along with the analytic result given by Eq. (12-17). The numerical model was integrated with $z_{G_{max}} = 10$ m, and m_3 was multiplied by 10^2 for comparison against the linear solution m_{3_a}. The results are almost coincident up to 10 km, thereby providing proof of the fidelity of the numerical model. Above 10 km, the numerical model uses an absorbing layer (see Section 11.3.2) to mimic the radiation boundary condition of the analytic model.

Another useful parameter that can be calculated from a model of forced air over rough terrain is the surface drag. This drag occurs because the sloping
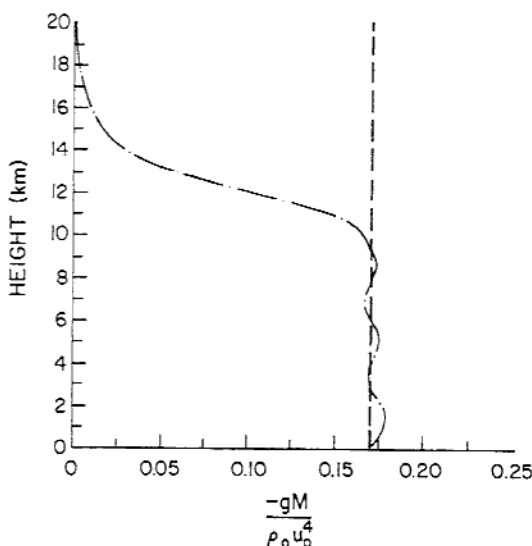

Fig. 12-12. A plot of m_3 calculated from Eq. (12-16) from a numerical model result for a bell-shaped mountain (dashed-dotted line) and m_{3_a} evaluated using Eq. (12-17) for the same mountain shape (dashed line), as a function of height for $u_0 = 20$ m s^{-1}, $z_{G_{max}}$ equivalent to 100 m, and $\rho_0 = 1$ kg m^{-3}. The atmosphere is isothermal, and M corresponds to m_3 and m_{3_a}. (Adapted from Klemp and Lilly 1978.)

terrain is a partial barrier and impedes the large-scale wind flow. The wave drag for a two-dimensional mountain can be written as

$$D = \int_{-\infty}^{\infty} \bar{p}(z_G) \frac{\partial z_G}{\partial x} \, dx, \qquad (12\text{-}18)$$

where $\bar{p}$ is evaluated on z_G. The momentum flux [Eq. (12-16)] evaluated at z_G is identical to the surface drag given by Eq. (12-18). The integrand of Eq. (12-18) arises from the force per unit area exerted on a two-dimensional mountain in the x direction.[7] For a mountain that is symmetric around its crest, for example, an asymmetric pressure field will result in a value of D that is not equal to 0. Moreover, since total energy must be conserved, the generation of internal gravity waves by a mountain must result in the extraction of energy from the ground.

From the Lilly and Klemp (1979) solution to Long's model presented in Section 5.3,

$$D_{LK} = -\rho_0 u_0^2 \int_{-\infty}^{\infty} \sigma \left(z_{G_i} - \left(\frac{\sigma z_{G_i}^2}{2} \right) \right) \frac{\partial z_G}{\partial x} \, dx, \qquad (12\text{-}19)$$

where the subscript "LK" indicates that it is from the Lilly–Klemp solution to the Long model. Lilly and Klemp (1979) contrast the drag [Eq. (12-19)] from their solution to Long's equation for an isothermal atmosphere with constant velocity using a nonlinear bottom boundary condition, with the drag [Eq. (12-17)] computed for a linear lower boundary condition. Among their results, they found that the drag was enhanced compared to linear theory for mountains with a gentle upslope and steep downslope terrain.

12.6   Comparison with Observations

The validation of a model using observations can be cataloged into two general classes: (1) subjective validation and (2) point and pattern quantitative validation. In subjective validation, one or more of the predicted fields are qualitatively compared against observations of a related phenomena. Pielke (1974a), for example, compared the simulated vertical motion at an elevation of 1.22 km over south Florida with the observed locations of rain showers as seen via a 10-cm radar located in Miami. The justification for the comparison is that the primary control for rain shower development over south Florida during a synoptically undisturbed summer day is the location and intensity of the low-level convergence (Pielke *et al.* 1991). Since 1.22 km is approximately at the top of the planetary boundary layer, the predicted vertical velocity at that level yields an appropriate estimate for low-level convergence. Figure 12-13 illustrates one such comparison for June 29, 1971, 9-1/2 hours after sunrise. As evident in the
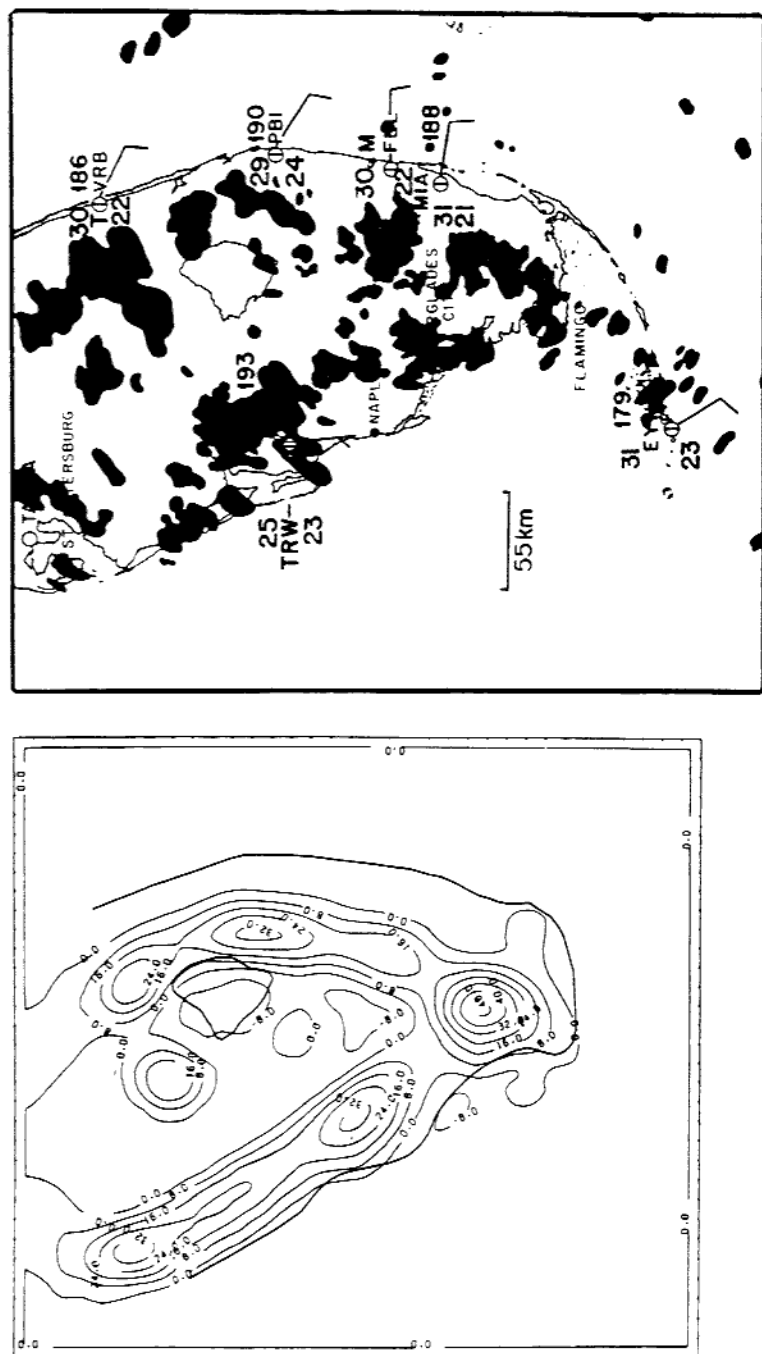
Fig. 12-13. A model-predicted vertical motion field at 1.22 km and the radar echo map at about 9.5 hours after sunrise for June 29, 1971. The large-scale horizontal velocity used in the model simulation above the initial height of the planetary boundary layer was 2.5 m s⁻¹ from the east-southeast. The model used in this simulation is reported in Pielke (1974a).

figure, the wishbone pattern of the rain showers is closely correlated with the distribution of vertical motion at 1.22 km.

Point-to-point correspondence between model prediction and observation of the same meteorological parameter provides a quantitative test of model skill. Keyser and Anthes (1977) use a technique in which if ϕ_i and $\phi_{i_{obs}}$ are individual predictions and observations at the same grid point, ϕ_0 and $\phi_{0_{obs}}$ are the average values of ϕ_i and $\phi_{i_{obs}}$ at a level, and #N is the number of observations, then

$$E = \left\{ \sum_{i=1}^{\#N} (\phi_i - \phi_{i_{obs}})^2 / \#N \right\}^{1/2},$$

$$E_{UB} = \left\{ \sum_{i=1}^{\#N} [(\phi_i - \phi_0) - (\phi_{i_{obs}} - \phi_{0_{obs}})]^2 / \#N \right\}^{1/2}, \qquad (12\text{-}20)$$

$$\sigma_{obs} = \left\{ \sum_{i=1}^{\#N} (\phi_{i_{obs}} - \phi_{0_{obs}})^2 / \#N \right\}^{1/2},$$

and

$$\sigma = \left\{ \sum_{i=1}^{\#N} (\phi_i - \phi_0)^2 / \#N \right\}^{1/2}$$

can be used to determine the skill of the model results. The parameter E is the *root mean square error* (RMSE), E_{UB} is the RMSE after a constant bias is removed, and σ and σ_{obs} are the standard deviations of the predictions and the observations, respectively.[8] Keyser and Anthes found that the RMSE can be significantly reduced when a constant bias is removed. Such a bias, they suggested, could result from incorrect specification of the initial and/or bottom and lateral boundary conditions.

Skill is demonstrated when (1) $\sigma \simeq \sigma_{obs}$, (2) $E < \sigma_{obs}$, and (3) $E_{UB} < \sigma_{obs}$. Pielke and Mahrer (1978) applied these criteria to their simulation of the sea breezes over south Florida to show that the model could accurately predict wind velocity and temperature at 3 m. Temperature predictions over the entire daylight period, as given in Table 12-1, for example, had a ratio of $E_{UB}/\sigma_{obs} = 0.6$. Segal and Pielke (1981) have applied this analysis tool over the Chesapeake Bay region to evaluate the accuracy of a mesoscale model prediction of biometeorological heat load during the daylight hours. For temperature, for example, Segal and Pielke found that $E/\sigma_{obs} = 0.53$ with $\sigma_{obs} = 2.12°C$ and $\sigma = 2.24°C$. This evaluation technique has also been applied by Shaw *et al.* (1997) in the modeling of a Great Plains dryline.

One problem with point-to-point validation, however, is that spatial and temporal displacement of the predicted from the observed fields could yield a poor verification according to Eq. (12-20), even though the shape and magnitude of the simulated pattern could be almost exact. Although not yet attempted in a

TABLE 12-1

Error Analysis of Model-Predicted Winds and Temperature Using Eq. (12-20) for an
East–West Cross-Section From Naples to Just North of Fort Lauderdale, Florida
(See Figure 12-13 for the Location)

Variable	E	E_{UB}	σ	σ_{obs}	E_{UB}/E	E_{UB}/σ_{obs}
$\bar{u}$ (m s^{-1})	3.1	3.1	1.2	2.2	1.0	1.4
$\bar{v}$ (m s^{-1})	2.2	1.2	0.8	1.2	0.5	1.0
$\bar{T}$ (°C)	5.1	2.8	3.9	4.6	0.5	0.6

From Pielke and Mahrer 1978.

mesoscale model, rigid translation of the predicted results on the model grid
(e.g., in one–grid-interval increments) relative to the observations, and recom-
putation of E and E_{UB} in Eq. (12-20), offers one possibility for considering the
effect of displacement on the accuracy of the results.

A quantitative measure of a model's ability to predict observed meteorological
fields, such as displayed in Figure 12-13, is also possible using concepts of set
theory. Pielke and Mahrer (1978) applied this technique to determine the degree
of correspondence between predicted low-level convergence zones (as estimated
by the vertical velocity, $\bar{w}$, at 1.22 km) and the locations of radar echoes over
south Florida. Two major questions were answered using this technique:

1. What fraction of the predicted convergence zones are covered by
showers?
2. What fraction of the showers that occur lie inside of the predicted con-
vergence zones?

To illustrate the procedure of analysis, let $D_x D_y$ be the model domain area, let
C be the area of the model domain covered by predicted convergence of a given
magnitude or larger, and let R be the area of the model domain covered by radar
echoes of a specified intensity and greater. With these definitions, the following
apply:

1. $F_E = (C \cap R)/R$ is the fraction of echoes in convergence zones with
values equal to or greater than a certain value of convergence (where the symbol
$\cap$ is an intersection in set theory symbolism).
2. $F_m = C/D_x D_y$ is the fraction of the model domain covered by a specified
value of convergence and larger.
3. $F_c = (C \cap R)/C$ is a measure of the fraction of convergence zones, of a
given magnitude and larger, covered by echoes.

Capability is demonstrated if $F_E/F_m > 1$, since the ratio would be expected
to be unity by random chance. A necessary condition for perfect skill is

$F_c = 1$, since in that case the entire convergence zone would be covered with echoes.[9]

This methodology is illustrated schematically in Figure 12-14 for an idealized distribution of radar echoes and convergence. Results for an actual model simulation of a sea breeze over south Florida (for July 1, 1973) from Pielke and Mahrer (1978) are given in Table 12-2, where the ratio of F_E/F_m was greater than unity in 26 out of 30 categories. The ratio was larger than 2.0 in 20 of the categories. In contrast, F_c was much less than unity, indicating that most of the convergence zones were not covered by rain showers—a result indicating that sea-breeze convergence alone does not completely explain the spatial variability of radar echoes over south Florida in the summer.

The application of this analysis procedure to other meteorological variables, such as cloud cover and rainfall, is straightforward. Simpson et al. (1980), for example, quantitatively examined the skill of the mesoscale model predictions over south Florida on several days during the summer to predict locations of shower mergers as seen by radar. This technique can, of course, be applied to other geographic areas and to different mesoscale systems.

Anthes (1983) provides an effective summary of additional evaluations of model capability. These include

$$TS = \frac{CFA}{FA + OA - CFA},$$

where TS is called the "threat score," CFA is the correctly forecast area, FA is the forecast area, and OA is the observed area. These quantities are equivalent to $CFA = C \cap R$, $FA = C$, and $OA = R$ used to obtain Table 12.2.
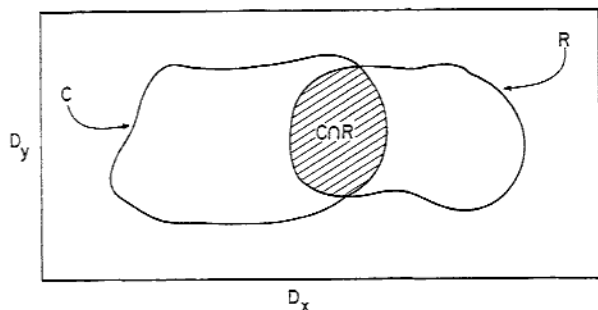
Fig. 12-14. A schematic illustration of the juxtaposition of a field of radar echoes R and low-level convergence of a given magnitude and larger C. The two fields are coincident at $C \cap R$. The quantity $F_c = (C \cap R)/C$ indicates the fraction of a convergence zone covered by radar echoes, and $F_E/F_m = [(C \cap R)/R]/(C/D_x D_y)$ measures the ratio of echoes within the convergence zone to the fraction of the model domain covered by that magnitude of convergence and larger.

TABLE 12-2

The Fraction of Convergence Zones F_c of a Given Magnitude and Larger, Covered by Radar Echoes, and the Ratio of the Fraction of Echoes in Convergence Zones of a Given Magnitude and Larger to the Fraction of the Model Domain Covered by that Magnitude of Convergence and Larger; This Ratio is Given by F_E/F_m.

Time (EST)	F_c					F_E/F_m				
	(i)	(ii)	(iii)	(iv)	(v)	(i)	(ii)	(iii)	(iv)	(v)
1200	0.0049	0.0118	0.0	0.0	0.0	1.31	2.67	0.0	–	–
1300	0.0571	0.1237	0.0072	0.0	0.0	2.16	3.17	0.20	–	–
1400	0.0945	0.1770	0.3111	0.0	0.0	1.98	2.78	3.50	0.0	–
1500	0.1396	0.1337	0.1942	0.3040	0.0	2.25	2.56	3.29	6.00	–
1600	0.0889	0.1765	0.1156	0.00	0.0	2.44	2.95	2.00	0.0	–
1700	0.1609	0.2829	0.2950	0.2379	0.0	2.49	3.16	3.00	2.33	–
1800	0.1451	0.1976	0.3403	0.3866	0.0909	2.19	3.07	3.75	3.75	0.10
1900	0.0759	0.1205	0.1313	0.0211	0.0	1.06	1.43	1.67	1.67	–

Convergence is defined by vertical velocity $\bar{w}$ at 1.22 km. For 1200–1800 EST. (i) $\bar{w} > 0$ cm s^{-1}, (ii) $\bar{w} > 8$ cm s^{-1}, (iii) $\bar{w} > 16$ cm s^{-1}, (iv) $\bar{w} > 24$ cm s^{-1}, (v) $\bar{w} > 32$ cm s^{-1}. For 1900 EST (i) $\bar{w} > 0$ cm s^{-1}, (ii) $\bar{w} > 8$ cm s^{-1}, (iii) $\bar{w} > 24$ cm s^{-1}, (iv) $\bar{w} > 40$ cm s^{-1}, (v) $\bar{w} > 56$ cm s^{-1}. (From Pielke and Mahrer 1978.)

The threat score can also be defined as

$$TS = C/(F + O - C),$$

where C is the number of locations in which a forecast is defined to be correct, F is the number of locations for which a forecast is made, and O is the number of locations that observed the forecast quantity.

A bias score. B. can be defined as

$$B = FA/OA$$

and by

$$B = F/O.$$

Colle et al. (1999) discuss the changes in bias scores as the spatial grid increment in the MM5 model is made smaller.

To assess model skill. Mielke (1984, 1991) introduced a new statistical evaluation scheme called the Multivariate Randomized Block Permutation (MRBP) procedure. His approach has the advantage in that regression relations and comparisons between model and observed data is based on the absolute value of the differences, rather than on the square of the distances.

A summary of the MRBP technique is provided in Lee et al. (1995) and is reproduced here. As described by Sheynin (1973), the initial known use of regression by Bernoulli (circa 1734) for astronomical problems involved the

least sum of absolute deviations (LADs) regression. The distance function associated with LAD regression is the common Euclidean distance between observed and predicted response values. Further work in developing LAD regression was accomplished by Boscovich (circa 1755), Laplace (circa 1789), and Gauss (circa 1809). Sheynin (1973) points out that Gauss developed linear programming for the sole purpose of estimating the parameters associated with LAD regression. Gauss consequently had to introduce the least sum of squared deviations (LSD) regression (also termed least squares regression), simply because calculus provided an efficient way to estimate the parameters associated with LSD regression. Thus LSD regression is a default procedure that was introduced only because Gauss lacked appropriate computational equipment for solving linear programming problems. The American mathematician and astronomer Bowditch (circa 1809) immediately attacked LSD regression because squared deviations unduly overemphasize questionable observations in comparison to the absolute deviations associated with LAD regression (Sheynin 1973).

The MRBP procedure developed by Mielke (1984, 1991) is based on the LAD regression. Specifically, MRBP randomly permutes the observed vector of values $(\vec{X})$ relative to the model-predicted vector of values $(\widetilde{\vec{X}})$ with the agreement measure, ρ, defined by

$$\rho = \frac{\mu_\delta - \delta}{\mu_\delta},$$ (12-21)

where $\delta = (1/n) \sum_{i=1}^{n} |\vec{X}_i - \widetilde{\vec{X}}_i|$ is the average distance between n-observed and model-predicted data pairs and μ_δ is the average value of δ over all $n!$ permutations. Note that the Euclidean distance between vector value pairs is used to evaluate the agreement measure, and that good predictions are associated with relatively small values of δ. The LAD regression used here is both multivariate (i.e., n vectors of two or more dependent variables may be involved) and nonlinear. The remaining problem is to determine whether a realized value of δ for observed and model-predicted values is due merely to chance. The standard measurement for this purpose is the P value; that is, the probability of obtaining a value of δ that is not larger than a realized value of δ given that each of the $n!$ values of δ occurs with equal probability. Although the exact calculation of all $n!$ values of δ is seldom computationally feasible, an approximate P value is based on the standardized test statistic given by

$$T = (\delta - \mu_\delta)/\sigma_\delta,$$ (12-22)

where σ_δ is the exact standard deviation of δ and T is approximately distributed as a Pearson type III distribution (Mielke 1984, 1991). Examples of the use of the MRBP evaluation technique in mesoscale modeling are reported in Cotton *et al.* (1994), Lee *et al.* (1995), and Mielke and Berry (2000).

12.7 Model Sensitivity Analyses

Stein and Alpert (1993) and Alpert *et al.* (1995) have introduced a very effective analysis procedure for assessing model sensitivity to the alteration of model formulations. These alterations, for example, could include integrating a model with surface latent turbulent heat fluxes excluded, as contrasted with a control run in which these fluxes are included.

When one alteration is contrasted with the control run, simply subtracting the two model runs at equivalent times of integrations is the obvious procedure for assessing the model's sensitivity to the alteration. However, when two alterations are evaluated (e.g., surface turbulent sensible heat fluxes are also excluded), the interaction between the two alterations must be assessed. Only if the alterations are not interactive (i.e., "orthogonal") to each other would running the two alteration experiments and then adding them together provide the model's sensitivity to the combined effect of both alterations.

The Stein–Alpert analysis procedure includes the effect of the interactions. Following this analysis procedure, if f_0 is the control and f_1, f_2, and f_3 represent three alteration experiments, then

$$\hat{f_1} = f_1 - f_0,$$
$$\hat{f_2} = f_2 - f_0,$$
$$\hat{f_3} = f_3 - f_0,$$

where $\hat{f_1}$, $\hat{f_2}$, and $\hat{f_3}$ represent the individual effects of making just one alteration to the control. In the past, this is where most sensitivity experiments ended. However, as shown by Stein and Alpert,

$$\hat{f}_{12} = f_{12} - (f_1 + f_2) + f_0,$$
$$\hat{f}_{13} = f_{13} - (f_1 + f_3) + f_0,$$
$$\hat{f}_{23} = f_{23} - (f_2 + f_3) + f_0$$

represent the interaction between each pair of alterations when two alterations from the control are made in the same experiment. When these alterations are made in the same experiment, the three-way interaction effect is

$$\hat{f}_{123} = f_{123} - (f_{12} + f_{13} + f_{23}) + (f_1 + f_2 + f_3) - f_0.$$

Examples of uses of the Stein–Alpert sensitivity analysis procedure are reported in Alpert *et al.* (1995, 1996a, 1999), DeRidder and Gallee (1998), Romero *et al.* (1998, 2000), Eastman (1999), Grossi *et al.* (2000), and Eastman *et al.* (2001).

Notes to Chapter 12

1. The other type of sensitivity study involves changes in the physical parameters within the model (e.g., initial wind speed, Coriolis value, ground roughness).

2. The solution to this diagnostic differential equation can be obtained using the procedure of sequential relaxation discussed in Section 10.3. Haltiner and Williams (1980, Chap. 5) also present procedures to solve Eq. (12-3) using direct matrix procedures. Mason and Sykes (1978) discuss the use of a direct method to solve for pressure in a Cartesian coordinate framework even when topography exists in the model domain.

Also, in deriving Eq. (12-2), the velocities on the right of Eq. (4-14), were assumed to be the velocities obtained when the complete nonhydrostatic pressure, $\bar{p}_H + R'$, was used (e.g., as available at the beginning of a time step). This assumption does not have to be made, however (it simply results in more terms in Eq. (12-3) if it is not made). As long as changes of R' at a grid point between time steps are small relative to the magnitude of R', it is a reasonable assumption.

3. If $u' \equiv 0$ at the boundaries, then $\partial u'/\partial x$ and $\partial u'/\partial t$ must also be identically 0 at these locations. Therefore, from Eq. (5-17), $g\partial h/\partial x = 0$ at the boundaries, so that no slope to the fluid is permitted at the walls. Numerical approximations to the tank model equations with rigid walls must use this boundary condition on h, recognizing that $\partial h/\partial x = 0$ at the boundary does not mean that $\Delta h/\Delta x = 0$ between the boundary and one grid point inside when Δx is finite.

4. As used here and in Section 6.3, s is a constant, usually defined to correspond to the initial value of s_θ as defined by Eqs. (11-13) and (11-19) and following material. The variable s_θ corresponds to a movable potential temperature surface.

5. As shown by Dutton (1976:144), differential area on a constant $\tilde{x}^3$ surface can be written as $dS = |\bar{n}^3|\sqrt{\tilde{G}}d\tilde{x}^2d\tilde{x}^1$. For the terrain-following coordinate system defined by Eq. (6-48), $\sqrt{\tilde{G}} = (s - z_G)/s$ [from Eqs. (6-32) and (6-51)] and for small slopes $|\bar{n}^3| \simeq s/(s - z_G)$ [from Eqs. (6-33) and (6-51)].

6. Leibnitz's rule is given in such sources as Hildebrand (1962:360) and Dutton (1976:115).

7. The change in force per unit area in the x direction can be written as $\bar{p}(z_G)\cos\alpha\Delta n/\Delta x$, where α is the terrain slope and Δn is distance along the slope. Since $\Delta n\cos\alpha = \Delta z$, at $z = z_G$, the change in force per unit area in the x direction becomes $\bar{p}(z_G)\Delta z_G/\Delta x$. In the limit as Δz_G and Δx approach 0, and integrating from + to $-\infty$ yields Eq. (12-18).

8. The use of RMSE analysis to examine the skill of model results for different sets of initial conditions was also discussed in Section 11.2 associated with Eq. (11-5).

9. Since R can be larger than C, $F_c = 1$ is not a sufficient measure of perfect skill.

Additional Readings

Several studies provide additional examples of model evaluations.

Cox, R., B. L. Bauer, and T. Smith. 1998. A mesoscale model intercomparison. *Bull. Amer. Meteor. Soc.* **79**, 265–283.

Hanna, S. R., and R. Yang. 2001. Evaluations of mesoscale models' simulations of near-surface winds, temperature gradients, and mixing depths. *J. Appl. Meteor.*, **40**, 1095–1104.

Snook, J. S., P. A. Stamus, J. Edwards, Z. Christidis, and J. A. McGinley. 1998. Local-domain mesoscale analysis and forecast model support for the 1996 Centennial Olympic Games. *Wea. Forecasting* **13**, 138–150.

Problems

1. Using the one-layer tank model programmed in problem 9 in Chapter 10, use the equations in Section 12.5.1 to compute the time rate of change of the mass and energy budget of the model by summing over the grid points of the model and then compare to what they should be from the requirement that h is a constant and Eqs. (12-5) and (12-7). Use cyclic lateral boundary conditions.

2. Repeat problem 1 with constant inflow and gradient outflow lateral boundary conditions.

3. Repeat problem 1 with constant inflow and radiative outflow lateral boundary conditions.

4. Select a mesoscale model and describe which of the model evaluations reported in this chapter have been used.